Synthesis of orientated $Ni_{0.89}Fe_{0.11}$/polymer nanofibres with a bimodal nanoparticle size distribution by electrospinning and thermal processing

T. Nawaz [a], G.V.M. Williams [a,*], M.P. Coles [a], A. Edgar [a], S.V. Chong [b]

[a] *School of Chemical and Physical Sciences, Victoria University of Wellington, PO Box 600, Wellington 6140, New Zealand*
[b] *Robinson Research Institute, School of Engineering, Victoria University of Wellington, PO Box 33436, Lower Hutt 5046, New Zealand*

ARTICLE INFO

ABSTRACT

Orientated ferromagnetic $Ni_{0.89}Fe_{0.11}$ nanoparticle/polymer nanofibres were made by electrospinning a solution containing iron(III) nitrate nonahydrate, nickel(II) acetate tetrahydrate, polyvinylpyrrolidone, and acetic acid in methanol and thermally processed in Ar and then 95%Ar:5%H_2 up to 620 °C. There was a distribution in nanofibre widths after electrospinning with wider (average width 440 nm) and some thinner (average width 120 nm) nanofibres. The nanofibre width distribution decreased after heat treatment and the average nanofibre width reduced to 160 nm. A bimodal $Ni_{0.89}Fe_{0.11}$ nanoparticle size distribution was found where there were large surface nanoparticles with a mean diameter of 35 nm and small inner nanoparticles with a 5 nm mean diameter. There was a small spin-disordered shell magnetization that was only ~2% of the total 5 K saturation magnetization and a characteristic spin-freezing temperature of 21 K. The high field magnetization was large, and it reached 41.7 Am^2/kg at 5 K.

1. Introduction

Magnetic nanofibres have been under increasingly intense investigation because of their actual and potential uses in a wide range of fields. These include applications in drug delivery [1], cancer detection and treatment [2,3], biomedical technologies [4], DNA separation [5], fuel cells [6–8], radio frequency (RF) shielding [9,10], non-volatile magnetic memory [11,12], microwave absorption [13,14], Li-ion batteries [15,16], solid oxide fuel cells [8], gas sensing [17], and magnetic sensors [18–20]. Thin nanowires can also potentially be used in domain wall magnetic memory [21,22]. Their advantages include large surface areas and being able to be produced in very thin sheets for compact devices. They can also have a large magnetic shape anisotropy, which is ideal for magnetic flux guiding applications that include magnetic sensors [18,19], thin RF antennae, and RF shielding [9,10]. The use of magnetic nanofibres for these and other similar applications is also advantageous because the eddy current losses are significantly reduced when compared with the bulk compounds. However, they can still display hysteresis losses due to effects that include domain wall motion.

One potential method to significantly reduce hysteresis losses in magnetic nanofibres is to create magnetic nanofibres composed of superparamagnetic nanoparticles. Superparamagnetic nanoparticles

display negligible hysteresis above the blocking temperature, T_B, where the thermal energy is greater than the magnetocrystalline anisotropy energy [23]. Thin layers of $Ni_{1-x}Fe_x$ nanoparticles are known to have negligible hysteresis above T_B while still maintaining a reasonable magnetic susceptibility [24]. Magnetic nanofibres composed of nanoparticles would also further reduce eddy current losses due to higher resistivities from enhanced carrier scattering and interparticle tunneling. There are also other potential applications that include zero power magneto-electric magnetic sensors when the polymer is piezo-electric (e.g. PVDF) [25]. Magnetic nanoparticles are known to display interesting physics that is different from the bulk. This includes the appearance of a gap in the magnon dispersion [26,27], changes in the magnetocrystalline anisotropy energy [28–30], enhanced magneto-striction [31] for nanoscale magneto-electric applications [25], and an exchange bias from spin-disordered shells that may be suitable for magnetic RAM. [20,32,33] They can also have enhanced coercivities that is useful for ultrahigh density magnetic storage [34].

Electrospinning is a promising method to achieve orientated, isotropic, and size variable magnetic nanofibers [35–38]. It has been used to make magnetic nanoparticle/polymer nanofibres by electrospinning a solution containing nanoparticles and a polymer [35] or by electrospinning metals containing precursor compounds and a polymer

---

followed by thermal processing [7,16,39] Incorporating magnetic nanoparticles in the polymer has been used to make electrospun FePt [40], and magnetite nanofibers [41,42]. Thermal processing of precursor solutions has been used to make different magnetic nanoparticle/polymer nanofibres including Ni_xCo_{1-x} nanoparticles [7,16], $NiFe_2O_4$ [39,43], and $CoFe_2O_4$ [44]. However, there have been no reports of bimetallic $Ni_{1-x}Fe_x$ nanoparticle/polymer nanofibres or nanorods. $Ni_{1-x}Fe_x$ is interesting because bulk $Ni_{1-x}Fe_x$ is used in magnetic flux guiding applications [45]. It can have a very low magnetocrystalline anisotropy for $x{\sim}0.26$ and hence $Ni_{1-x}Fe_x$ nanoparticles with sizes up to $\sim$60 nm could potentially have a T_B lower than 300 K and magnetic susceptibilities > 1000 [46].

In this paper, we report the synthesis of orientated ferromagnetic $Ni_{0.89}Fe_{0.11}$/polymer nanofibres made by electrospinning followed by heating in an Ar atmosphere and further reduction up to 620 °C in a 95% Ar:5%H_2 atmosphere. This method was chosen over direct $Ni_{1-x}Fe_x$ nanoparticle incorporation because of the potential for novel nanoparticle size distributions and morphologies. We observed a bimodal particle size distribution, where large $Ni_{1-x}Fe_x$ nanoparticles occurred at the surface and smaller $Ni_{1-x}Fe_x$ nanoparticles were embedded within the polymer. These nanofibers displayed a high saturation magnetization with a very small spin-disordered shell.

2. Experimental details

2.1. Materials

All chemicals used were of analytical grade. The chemical reagents iron(III) nitrate nonahydrate ($Fe(NO_3)_3 \cdot 9H_2O$, purity > 98%), nickel(II) acetate tetrahydrate ($Ni(CH_3CO_2)_2 \cdot 4H_2O$, purity 98%), and fine polyvinylpyrrolidone (PVP) powder (molecular weight of 1,300,000) were from Sigma-Aldrich. Acetic acid (99.7% purity) was from PanReac AppliChem. Methanol was obtained from Chem Supply.

2.2. Method

The nanofibre synthesis was based on a modified method described elsewhere [8,38,47]. A precursor solution was made by first separately dissolving 6 mmol of iron nitrate nonahydrate and 9 mmol of nickel acetate in 10 mL of methanol. Then 4 mL of the Ni acetate solution was transferred into a reaction vessel followed by the addition of 1 mL of acetic acid. The acetic acid was added prior to the addition of iron nitrate in this modified method to prevent the oxidation of Fe^{3+} in the basic solution. 1 mL of the Fe nitrate nonahydrate solution was added to the reaction mix to obtain a Ni/Fe stoichiometric ratio of 86:14. 0.25 g (2.25 mmol) of PVP was added to the solution while continuously stirring for 1 h to get a clear brown solution. Finally, this clear solution was loaded into a plastic syringe fitted with a 21-gauge stainless steel needle attached to a syringe pump (Harvard Apparatus) in a home-made electrospinning system. This whole set up was connected to a high-voltage power supply (Gamma High Voltage Research, Ormand Beach, FL). A rotating drum was used for the collection of continuously aligned nanofibres, and it was connected to the high-voltage power supply's earth electrode. A thin aluminum sheet was wrapped around the 15 cm diameter drum to enable collection of the nanofibres. The solution was pumped at an infusion rate of 0.4 mL/hr with an applied voltage of 12.5 kV and the drum was rotated at 60 rpm. The distance from the tip of the needle to the rotating drum was 10 cm. The nanofibrous mat was collected from the rotating drum after electrospinning and processed in a tube furnace. The temperature was ramped to 300 °C at a rate of 5 °C/min and held at 300 °C in an argon atmosphere for 2 h. This step was chosen to ensure removal of the solvent and any residual water from hydrated metal salt precursors. The gas was then changed to 95%Ar:5% H_2 followed by ramping at a rate of 5 °C/min to 620 °C, holding at 620 °C for 2 h, decreasing the temperature to 300 °C at a rate of 5 °C/min, and finally the furnace cooled to room temperature. Higher

temperatures were not possible due to melting of the aluminum sheet. The argon/hydrogen mixture was used to ensure the reduction of Fe and Ni and it is commonly used in making metallic nanofibres by electrospinning [20].

2.3. Characterization

Powder X-ray power diffraction (XRD) was carried out on a Bruker D8 diffractometer using Co K_α radiation (λ = 1.7890 Å). Scanning electron microscopy (SEM) was performed using a Jeol SEM-6500 to study the morphology of the sample. Energy dispersive X-ray spectroscopy (EDXS) was performed on the same instrument to determine the elemental composition of the sample. Transmission electron microscopy (TEM) and scanning transmission electron microscopy (STEM) mapping were carried out on a Jeol TEM-2100. ImageJ analysis of the SEM and TEM images was used to determine the average directions and widths of the fibers and the nanoparticles size distributions. The *a*-axis lattice parameter was calculated from the *d*-spacings of the XRD reflections for face centered cubic $Ni_{1-x}Fe_x$ given by the Eq. (1), where (h k l) are the Miller indices. The TEM electron diffraction patterns were also analysed using Eq. (1).

$$\frac{1}{d^2} = \frac{(h^2 + k^2 + l^2)}{a^2} \tag{1}$$

Thermal gravimetric analysis (TGA) measurements were performed using an SDT-Q600 with platinum pans. The samples were heated in Ar with a heating rate of 20 °C/min. A small piece of the electrospun sample was removed from the aluminum sheet before the TGA measurement. Magnetic measurements were performed using a magnetic property measurement system (MPMS) from *Quantum Design*. The sample was sealed in a gelatine capsule and placed inside a straw before being loaded into the MPMS for the magnetic measurements.

3. Results and discussion

The results from TGA measurements in Ar for pure PVP powder are plotted in Fig. 1(a). The initial weight was 22.8 mg. The TGA data shows an initial weight loss from ambient temperature to $\sim$140 °C due to evaporation of adsorbed moisture. This is followed by a nearly constant weight to $\sim$350 °C and then a slow decrease in weight to $\sim$390 °C, after which there is a rapid weight loss with a maximum slope at $\sim$440 °C. The rapid weight loss can be attributed to thermal degradation via pyrolysis of the PVP. The remaining weight percentage is 5.9% at 485 °C and this decreases slowly and continually to 5.1% at 550 °C where the residual product was a black carbonaceous film. These results are similar to those reported when PVP is heated in nitrogen [48,49].

Fig. 1(b) is a plot of the TGA data from measurements on the electrospun nanofibrous mat containing the precursor sample in Ar. The
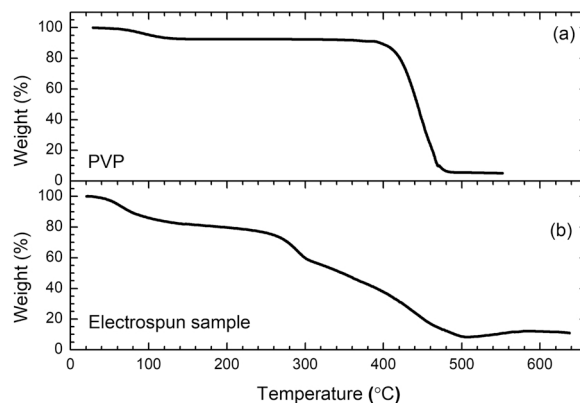

Fig. 1. TGA of (a) PVP powder and (b) the electrospun sample in Ar with a heating rate of 20 °C/min.

initial weight was 0.784 mg. Similar to the PVP results, there is an initial weight loss from ambient temperature to ~140 °C due to methanol and water evaporation. However, unlike PVP, there is a gradual weight loss to ~230 °C followed by a more rapid drop with a maximum slope at ~285 °C. This may be due to partial degradation of the acetate in the presence of the oxidizing nitrate. There is a more gradual and continual weight loss from ~300 °C to ~500 °C due to the degradation of PVP that is enhanced by the oxidizing nitrate and oxygen products from the thermal decomposition of acetate. The remaining weight percentage above 500 °C is ~10%. There are small weight changes above 500 °C where the weight percentage is 8.2% at 507 °C and reaching 12.2% at 586 °C. The actual weight change is only 0.016 mg and hence it likely to be instrument related. The material in the pan after the TGA measurement consisted of a small black ball.

SEM micrographs are shown in Fig. 2 of the nanofibres after electrospinning and before thermal processing. It is apparent in Fig. 2(a) that there is a general orientation of the nanofibres. There is no evidence for branching, connected fibers, or beading, and Fig. 2(b) clearly shows that the surfaces are very smooth. The nanofibres are not cylindrical but are shaped more like nanoribbons. There is a distribution in the nanofibre widths where there are wide and some narrow nanofibres. The distribution of the widths for the wider nanofibres is plotted in the inset to Fig. 2(a) where the average width is 440 nm. The thinner nanofibres have an average width of 120 nm.

Thermal processing leads to a significant change in the nanofibres and the formation of nanoparticles. This is apparent in Fig. 3(a) that shows a SEM image after thermal processing where small nanoparticles can clearly be seen at the surface of the nanofibres. There was also a large reduction in the nanofibre widths as can be seen in the inset to Fig. 1(a) where the average nanofibre width was 160 nm. Furthermore, the range in nanofibre widths had also reduced where the standard deviation was 100 nm before and 40 nm after thermal processing. However, the general nanofibre orientation has been retained. The average direction of the nanofibres is shown by the arrow in Fig. 3(a). Some small broken nanofibres are also evident in the image. The total percentage of Fe and Ni within these nanofibres was estimated by EDXS from three different areas. The Ni and Fe atomic fractions were 0.89 ± 0.02 and 0.11 ± 0.02, respectively. These are close to the expected Ni and Fe fractions from the starting material.

TEM images of a single 200 nm wide nanofibre in Fig. 3(b) and (c) provide more detailed information about the nanoparticles. There is a bimodal particle size distribution with large nanoparticles on the surface. A detailed examination of Fig. 3(c) shows that there are smaller nanoparticles that do not protrude through the surface suggesting that they are within the nanofibre. The nanoparticle size distributions are plotted in the inset to Fig. 3(c) for the small and Fig. 3(d) for the large nanoparticles using 3(b) and 3(c) and other TEM images. The average size of large nanoparticles was 35 nm, and the smaller nanoparticles had an average diameter of 5 nm.

The electron diffraction image in Fig. 4 shows that the nanoparticles that appear after thermal processing are $Ni_{1-x}Fe_x$. Four diffraction rings can clearly be seen, and they can be indexed to face centered cubic $Ni_{1-x}Fe_x$ where the Miller indices are (111), (200), (220), and (311) with increasing radius from the center spot. The lattice parameter was calculated from the d-spacings to be 3.53 ± 0.02 Å, which is in the range expected for $Ni_{1-x}Fe_x$ with low x [50,51]. The bimodal nanoparticle size distribution is also evident in the electron diffraction image where the bright spots are from the larger nanoparticles and the more diffuse spots and rings are from the smaller nanoparticles.

Fig. 5(a) is a TEM image of one of the fibers and the elemental maps from STEM mapping are shown in Fig. 5(b) to (f). It is apparent from the Ni and Fe STEM maps that the nanoparticles contain Ni and Fe, which is consistent with the formation of $Ni_{1-x}Fe_x$ nanoparticles. Fig. 5(d) is a carbon STEM map, and it shows that a carbon containing component is still present, which has prevented aggregation of the nanoparticles. The carbon maps have a reduced density in regions that correspond to the dark areas in the TEM image in Fig. 5(a) from the larger nanoparticles protruding from the surface. However, this is not the case for smaller nanoparticles suggesting that they are within the nanofibre. There is also some oxygen and nitrogen that is evident from Fig. 5(e) and 5(f). They are likely to be functional groups in the remaining PVP fragments. Some oxygen can be seen at the edges of the nanoparticle surfaces that could indicate a $NiFe_yO_z$ shell.

The XRD data are plotted in Fig. 6. The first two broad reflections are from the polymer within the sample and it is similar to the XRD data of PVP reported in the literature [52]. The two sharper reflections at higher angles can be indexed to the $Ni_{1-x}Fe_x$ face centered cubic crystal structure, that is expected for $x < 0.6$ [53]. The fitted lattice parameter was 3.534 ± 0.002 Å. It is the same as that found from the analysis of the electron diffraction data within the experimental uncertainty. The average particle size estimated from the Scherrer equation and using the (111) peak width was 39 nm. This is comparable to that estimated from the TEM data for the larger nanoparticles that are expected to dominate the XRD peak linewidth. This indicates that the $Ni_{1-x}Fe_x$ nanoparticles are not polycrystalline because such nanoparticles would have an average particle size from the Scherrer equation that is significantly smaller than the TEM average nanoparticle size.

The formation of $Ni_{1-x}Fe_x$ nanoparticles is likely to be via Ostwald ripening [54]. This is a nanoparticle growth process that is driven by a reduction in the total surface free energy where nanoparticles larger than a critical radius, R_c, grow and those less that R_c dissolve in the surrounding matrix [54]. The rate of nanoparticle growth depends on the Ni and Fe diffusivities [54]. Thus, the appearance of smaller nanoparticles within the nanofibres indicates that the Ni and Fe diffusivities in the presence of the remaining PVP fragments are lower than that in the surface region. One mechanism by which that can occur is the effect of functional groups (e.g. $-C=O$) from the residual polymeric fragments that strongly bind to the Fe^{3+} and Ni^{2+} ions. It is also possible that the
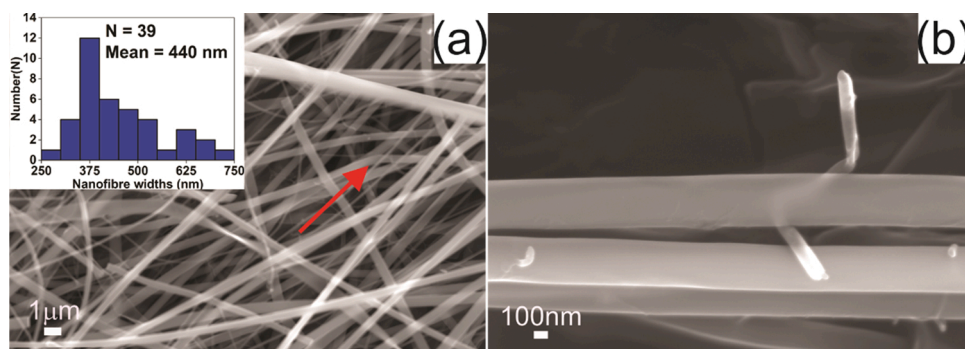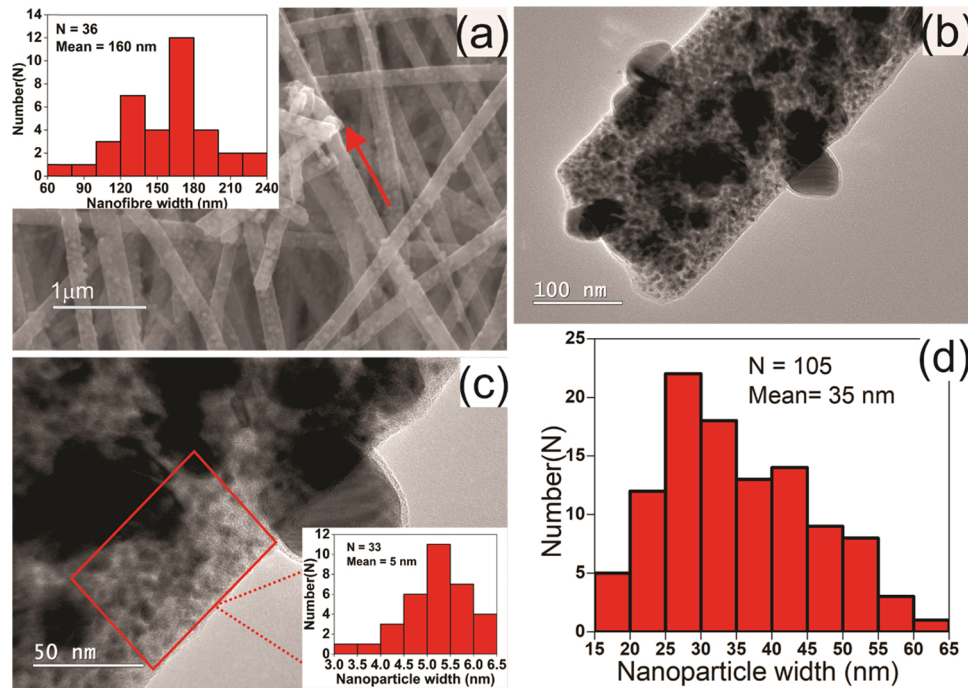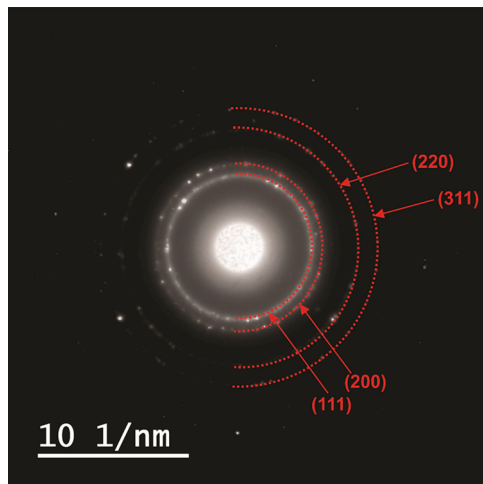

Fig. 2. SEM images of the sample after electrospinning at (a) low resolution and (b) high resolution. The arrow in (a) is a guide to the eye to indicate the general nanofibre direction. The inset to (a) is the nanofibre width distribution obtained from (a) and other SEM images.

Fig. 3. (a) SEM image after thermal processing. The arrow in (a) is a guide to the eye and indicates the average nanofibre direction. The inset is the nanofibre width distribution. (b, c) TEM of a single nanofibre from the thermally processed sample. The inset in (c) is the nanoparticle size distribution for the smaller nanoparticles within the selected area. (d) The nanoparticle size distribution for the larger nanoparticles from (b) and other TEM images.

Fig. 4. Electron diffraction image of a single nanofibre from the thermally processed sample. Electron diffraction was done on the sample area shown in Fig. 3(b). The dashed half circles are the Miller indices (111), (200), (220), and (311) for face centered cubic $Ni_{1-x}Fe_x$.

PVP fragments are less dense or shorter near the surface when compared with the interior, which could lead to larger near-surface Ni and Fe diffusivities. The formation of surface nanoparticles and their aggregation to form large clusters of nanoparticles is unlikely. This is because it would lead to polycrystalline nanoparticles with an average particle size estimated from the Scherrer equation that is significantly less than the average size from TEM, which is not the case.

The results from magnetic measurements can be seen in Fig. 7. The main graph shows the magnetization plotted against the applied magnetic field at 5 K and 300 K. The magnetization starts to saturate above ~0.7 T, which is consistent with the ferromagnetic order expected for $Ni_{1-x}Fe_x$ where the Curie temperature is far above room temperature. The high field magnetization is 41.7 Am^2/kg (emu/g) at 5 K. This is less

than that expected for bulk Ni (~60 Am^2/kg) or $Ni_{0.89}Fe_{0.11}$, where the bulk high field magnetization is ~90 Am^2/kg [53]. Part of the reason for the lower magnetization is due the unknown weight of the polymer matrix and hence the high field magnetization from only $Ni_{0.89}Fe_{0.11}$ is expected to be larger than the measured 41.7 Am^2/kg. Other reasons include effects such as broken bonds, vacancies, surface strain, and oxidation of the shell that become more important as the nanoparticle size is reduced [55,56]. The measured high field magnetization from other $Ni_{1-x}Fe_x$ nanoparticles with x ranging from 0.1 to 0.25 is also lower than the bulk values [53,54,57–59]. Ni nanorods made by electrospinning also have lower saturation magnetizations that are ~42% of the bulk values [20,60,61].

The upper left inset in Fig. 7 shows the magnetization plotted over a smaller magnetic field range. The coercive field is 31 mT at 5 K and 12 mT at 300 K. The appearance of hysteresis at 300 K indicates that there are some nanoparticles that are too big to be superparamagnetic. While the ~5 nm nanoparticles are small enough to exhibit superparamagnetism [24,46,62], the ~35 nm nanoparticles are too large, and it is the larger nanoparticles that lead to hysteresis even at 300 K. The coercive field at 300 K is higher than that reported in bulk unannealed Ni (3 mT) [63] and Ni nanofibres [61]. However, it is similar to that reported for $Ni_{1-x}Fe_x$ nanoparticles with $x = 0.2$ and diameters of ~15 nm (12 mT) [54,57] and $x = 0.25$ with diameters of 23 nm (~10 mT) [58]. It is twice of that reported for 18 nm diameter $x = 0.1$ nanoparticles (6 mT) [64].

The lower right inset to Fig. 7 shows the magnetization at 6 T, M (6 T), plotted against temperature. The saturation magnetization, M_s, in bulk $Ni_{1-x}Fe_x$ has a Bloch temperature dependence that can be written as $M_s(T) = M_s(0) \times [1 - \beta \times T^n]$ where $M_s(0)$ is the magnetization at zero Kelvin, β is the Bloch constant, T is the temperature, and $n = 3/2$ [65]. The Bloch temperature dependence can be derived assuming a quadratic magnon dispersion where β is proportional to $D^{-3/2}$ and D is the spin stiffness that is proportional to the exchange constant [29,66].

It is apparent in the lower right inset to Fig. 7 that there is departure from the Bloch temperature dependence at low temperatures where M_s shows an upturn below ~30 K. A similar departure also occurs in other
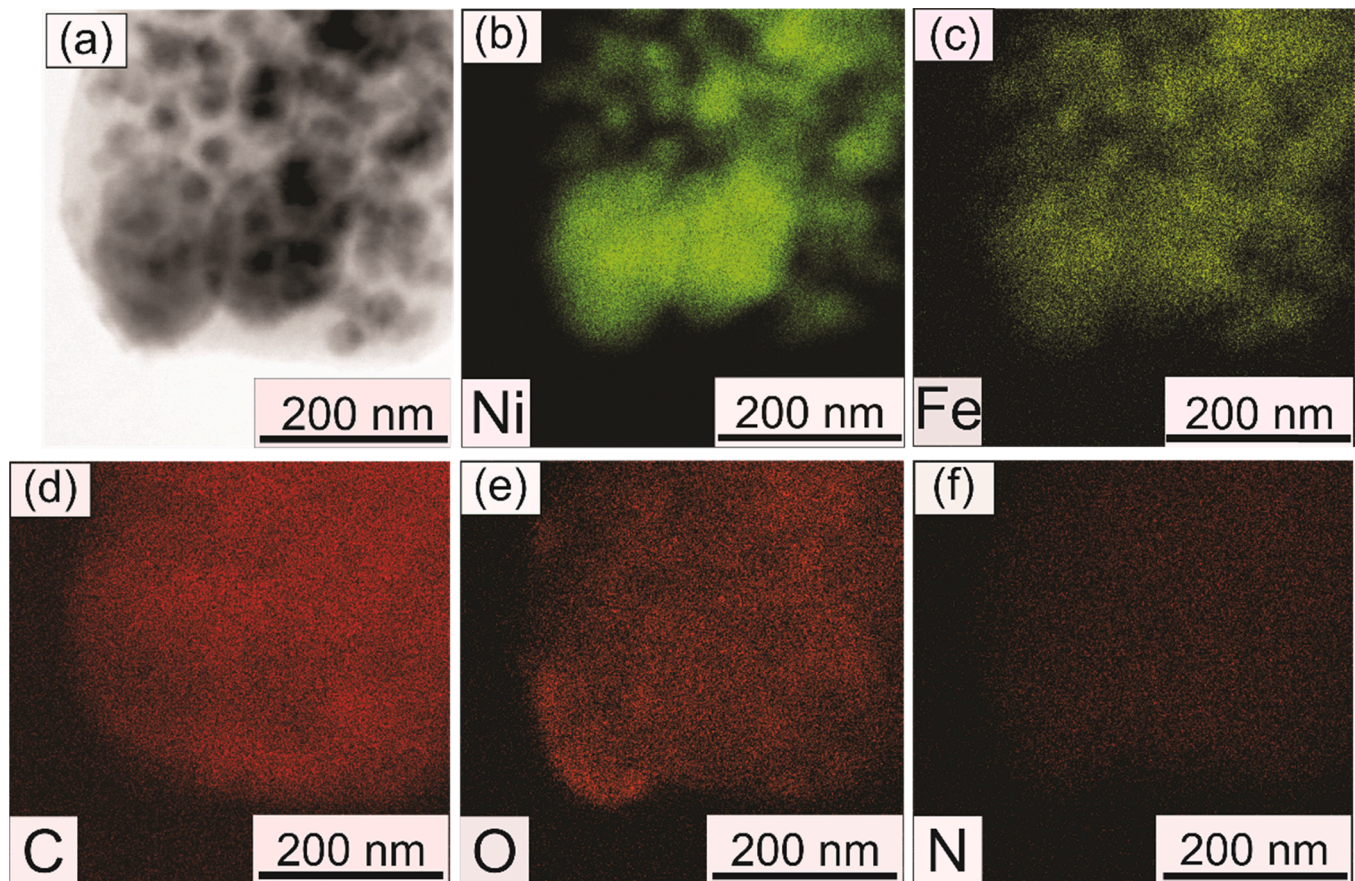
Fig. 5. (a) TEM image of part of a thermally processed nanofibre and (b to f) STEM maps of different elements from the same area.
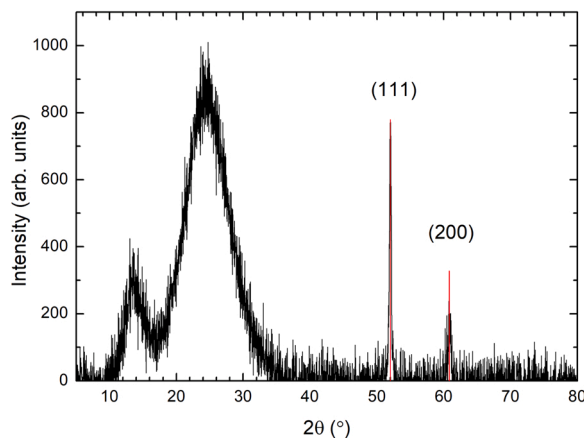

Fig. 6. XRD data after thermal processing. The vertical lines are fits to the maximum angles of the (111) and (200) reflections. The intensities are scaled using the Ni ICDD reference pattern number 00-004-0850, which is the closest reference pattern to $Ni_{0.89}Fe_{0.11}$.

Fig. 7. Plot of the magnetization against the magnetic field, *B*, at 5 K (black curve) and 300 K (blue curve) after thermal processing. Upper left inset: a plot of magnetization over a smaller magnetic field range. Lower right inset: a plot of the magnetization at 6 T against temperature (black curve). Also shown is a fit to the data using Eq. (2) (red dashed curve).

ferromagnetic nanoparticles [24,67,68] and has been attributed to the presence of a spin-disordered shell. The effect of spin-disorder on M_s can be modeled by including a phenomenological spin-disorder term [67, 68] leading to,

$$M_s(T) = M_{s,c}(0) \times [1 - \beta \times T^n] + M_{s,d}(0) \times \exp\left(\frac{-T}{T_f}\right) \quad (2)$$

where the first term is from the spin-ordered core and described using the Bloch function and the second term is from a spin-disordered shell.
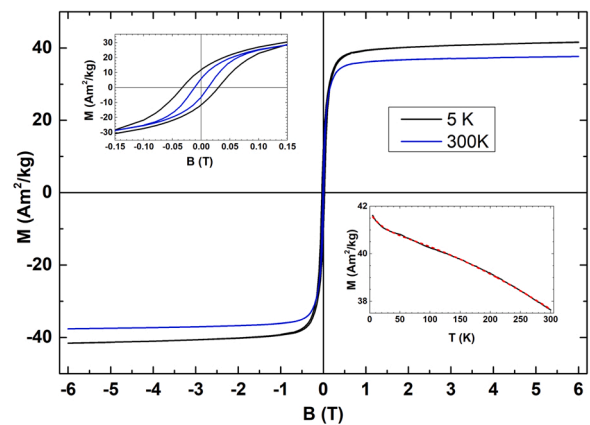
$M_{s,c}(0)$ is the spin-ordered core saturation magnetization at 0 K, $M_{s,d}(0)$ is the saturation magnetization from the spin-disordered shell at 0 K, and T_f is a characteristic spin-freezing temperature.

It can be seen in the lower right inset to Fig. 7 that Eq. (2) provides a good fit to the M(6 T) data with $n = 3/2$ that is expected for bulk ferromagnetic $Ni_{1-x}Fe_x$. The fitted β is 1.53×10^{-5} K$^{-3/2}$. It is an order of magnitude larger than that found in bulk Ni (7.5×10^{-6} K$^{-3/2}$) or bulk Fe (3×10^{-6} K$^{-3/2}$) [69–71]. However, β is known to be larger in magnetic nanoparticles [18,55,56]. It is in the range reported from studies on

other $Ni_{1-x}Fe_x$ nanoparticles. For example, it is 3.1×10^{-5} K$^{-3/2}$ for ~ 2.7 nm $Ni_{0.8}Fe_{0.2}$ nanoparticles and 3.8×10^{-5} K$^{-3/2}$ for ~ 4.6 nm $Ni_{0.8}Fe_{0.2}$ nanoparticles made by dual ion beam implantation [24], and it is 1.2×10^{-5} K$^{-3/2}$ for 35 nm $Ni_{0.5}Fe_{0.5}$ nanoparticles [70]. The fitted T_f is 21 K and it is in the range of values reported for dual ion implanted $Ni_{1-x}Fe_x$ nanoparticles with x ranging from 0.20 to 0.56 where T_f is between 17 K and 36 K. $M_{s,c}$(6 T,0 K) is 40.92 Am^2/kg (emu/g) and it is far greater than $M_{s,d}$(6 T,0 K) of 0.82 Am^2/kg (emu/g), which indicates that the spin-disordered shell is very thin.

4. Conclusion

In conclusion, orientated nanofibres containing ferromagnetic $Ni_{0.89}Fe_{0.11}$ nanoparticles and residual polymer were synthesized by electrospinning a mixture of iron(III) nitrate nonahydrate, nickel(II) acetate tetrahydrate, and polyvinylpyrrolidone in a solution containing acetic acid and methanol followed by thermal processing. The as-spun nanofibres had a distribution in widths where there were wider nanofibres with an average width of 440 nm and some thinner nanofibres with an average width of 120 nm. Thermal processing in argon up to 300 °C and then in 95%Ar:5%H$_2$ up to 620 °C led to nanofibres with $Ni_{0.89}Fe_{0.11}$ nanoparticles and residual polymer. This also resulted in a reduction in the average nanofibre width to 160 nm as well as a decrease in the nanofibre width distribution. The nanoparticles were found to have an unusual bimodal particle size distribution with smaller nanoparticles (5 nm) in the polymer matrix and larger nanoparticles at the surface (35 nm). The formation of larger nanoparticles at the surface indicates that the Ni and Fe diffusivities were higher in the nanofibre surface region when compared with the nanofibre interior. The lower diffusivities inside the nanofibres could be due to the effect of polymeric groups (e.g. $-C\!\!=\!\!O$) binding strongly to the Fe^{3+} and Ni^{2+} ions as well as PVP fragments that may be denser or longer within the nanofibres. Elemental maps showed that the nanoparticles were $Ni_{1-x}Fe_x$ and there was no evidence for separate Fe or Ni nanoparticles. There was oxygen surrounding some of the nanoparticles that may be due to a $NiFe_yO_z$ shell. The high field magnetization was large (41.7 Am^2/kg at 5 K), but less than that reported for bulk $Ni_{0.89}Fe_{0.11}$ where some of the difference is due to the mass of the polymer matrix. The Bloch constant was larger than that expected for bulk Ni or Fe but in the range reported for $Ni_{1-x}Fe_x$ nanoparticles. There was evidence for a thin spin-disordered shell with a characteristic spin freezing temperature of 21 K that could arise from a thin oxidized region.

Declaration of Competing Interest

The authors declare that they have no known competing financial interests or personal relationships that could have appeared to influence the work reported in this paper.

Acknowledgements

References

[1] E. Kaniukov, A. Shumskaya, D. Yakimchuk, A. Kozlovskiy, I. Korolkov, M. Ibragimova, M. Zdorovets, V. Rusakov, M. Fadeev, E. Lobko, K; Saunina, L. Nikolaevich, FeNi nanotubes: perspective tool for targeted delivery, Appl. Nanosci. 9 (5) (2018) 835–844.
[2] M.F. Contreras, R. Sougrat, A. Zaher, T. Ravasi, J. Kosel, Non-chemotoxic induction of cancer cell death using magnetic nanowires, Int. J. Nanomed. 10 (2015) 2141–2153.
[3] W. Hong, S. Lee, H.J. Chang, E.S. Lee, Y. Cho, Multifunctional magnetic nanowires: a novel breakthrough for ultrasensitive detection and isolation of rare cancer cells from non-metastatic early breast cancer patients using small volumes of blood, Biomaterials 106 (2016) 78–86.
[4] Y.P. Ivanov, A. Alfadhel, M. Alnassar, J.E. Perez, M. Vazquez, A. Chuvilin, J. Kosel, Tunable magnetic nanowires for biomedical and harsh environment applications, Sci. Rep. 6 (2016) 24189.
[5] J.-H. Nam, Y.-H. Joo, J.-H. Lee, J.H. Chang, J.H. Cho, M.P. Chun, B.I. Kim, Preparation of NiZn-ferrite nanofibers by electrospinning for DNA separation, J. Magn. Magn. Mater. 321 (10) (2009) 1389–1392.
[6] F. Guo, K. Cheng, K. Ye, G. Wang, D. Cao, Preparation of nickel-cobalt nanowire arrays anode electro-catalyst and its application in direct urea/hydrogen peroxide fuel cell, Electrochim. Acta 199 (2016) 290–296.
[7] N.A.M. Barakat, M. Motlak, A.A. Elzatahry, K.A. Khalil, E.A.M. Abdelghani, Ni$_x$Co$_{1-x}$ alloy nanoparticle-doped carbon nanofibers as effective non-precious catalyst for ethanol oxidation, Int. J. Hydrog. Energy 39 (1) (2014) 305–316.
[8] S. Lee, J.H. Park, K.T. Lee, Y.-W. Ju, Anodic properties of Ni-Fe bimetallic nanofiber for solid oxide fuel cell using LaGaO3 electrolyte, J. Alloy. Compd. (2021) 875.
[9] R. Han, W. Li, W.W. Pan, M.G. Zhu, D. Zhou, F.S. Li, 1D magnetic materials of Fe3O4 and Fe with high performance of microwave absorption fabricated by electrospinning method, Sci. Rep. (2014) 4.
[10] M. Bayat, H. Yang, F.K. Ko, D. Michelson, A. Mei, Electromagnetic interference shielding effectiveness of hybrid multifunctional Fe3O4/carbon nanofiber composite, Polymer 55 (3) (2014) 936–943.
[11] M. Pousthomis, E. Anagnostopoulou, I. Panagiotopoulos, R. Boubekri, W. Fang, F. Ott, K.A. Atmane, J.-Y. Piquemal, L.-M. Lacroix, G. Viau, Localized magnetization reversal processes in cobalt nanorods with different aspect ratios, Nano Res. 8 (7) (2015) 2231–2241.
[12] E. Cisternas, J. Faúndez, E.E. Vogel, Stabilization mechanisms for information stored in magnetic nanowire arrays, J. Magn. Magn. Mater. 426 (2017) 588–593.
[13] J. Xiang, X. Zhang, Q. Ye, J. Li, X. Shen, Synthesis and characterization of FeCo/C hybrid nanofibers with high performance of microwave absorption, Mater. Res. Bull. 60 (2014) 589–595.
[14] Y. Li, M. Yuan, H. Liu, G. Sun, In situ synthesis of CoFe$_2$O$_4$ nanocrystals decorated in mesoporous carbon nanofibers with enhanced electromagnetic performance, J. Alloy. Compd. (2020) 826.
[15] Z. Dai, H. Ke, Z. Long, R. Li, C. Shi, X. Su, H. Qiao, K. Wang, K. Liu, Facile synthesis and high lithium storage properties of mesoporous polypyrrole coated CoFe$_2$O$_4$ nanofibers, J. Alloy. Compd. (2021) 858.
[16] J. Huang, B. Zhang, Y.Y. Xie, W.W.K. Lye, Z.-L. Xu, S. Abouali, M.; Akbari Garakani, J.-Q.; Huang, T.-Y.; Zhang, B.; Huang, J.-K. Kim, Electrospun graphitic carbon nanofibers with in-situ encapsulated Co–Ni nanoparticles as freestanding electrodes for Li–O$_2$ batteries, Carbon 100 (2016) 329–336.
[17] P.V. Morais, P.H. Suman, R.A. Silva, M.O. Orlandi, High gas sensor performance of WO$_3$ nanofibers prepared by electrospinning, J. Alloy. Compd. (2021) 864.
[18] C. Zet, C. Fosalau, Magnetic nanowire based sensors, Dig. J. Nanomater. Biostruct. 7 (1) (2012) 299–306.
[19] B. Cox, D. Davis, N. Crews, Creating magnetic field sensors from GMR nanowire networks, Sens. Actuators A Phys. 203 (2013) 335–340.
[20] H. Wu, R. Zhang, X.X. Liu, D.D. Lin, W. Pan, Electrospinning of Fe, Co, and Ni nanofibers: synthesis, assembly, and magnetic properties, Chem. Mater. 19 (14) (2007) 3506–3511.
[21] S.S.P. Parkin, M. Hayashi, L. Thomas, Magnetic domain-wall racetrack memory, Science 320 (5873) (2008) 190–194.
[22] I. Polenciuc, A.J. Vick, D.A. Allwood, T.J. Hayward, G. Vallejo-Fernandez, K. O'Grady, A. Hirohata, Domain wall pinning for racetrack memory using exchange bias, Appl. Phys. Lett. 105 (2014) 16.
[23] B.D. Cullity, C.D. Graham. Introduction to Magnetic Materials, second ed, IEEE/Wiley, Hoboken, N.J, 2011.
[24] G.V.M. Williams, J. Kennedy, P.P. Murmu, S. Rubanov, S.V. Chong, The effect of different Fe concentrations on the structural and magnetic properties of near surface superparamagnetic Ni$_{1-x}$Fe$_x$ nanoparticles in SiO$_2$ made by dual low energy ion implantation, J. Magn. Magn. Mater. 473 (2019) 125–130.
[25] S.V. Chong, G.V.M. Williams, Magnetoelectric effect in magnetostrictive-piezoelectric composites containing magnetite nanoparticles, Sens. Actuators A Phys. 288 (2019) 101–106.
[26] P.V. Hendriksen, S. Linderoth, P. Lindgard, Finite-size modifications of the magnetic properties of clusters, Phys. Rev. B Condens. Matter 48 (10) (1993) 7259–7273.
[27] K. Maaz, A. Mumtaz, S.K. Hasanain, M.F. Bertino, Temperature dependent coercivity and magnetization of nickel ferrite nanoparticles, J. Magn. Magn. Mater. 322 (15) (2010) 2199–2202.
[28] X. Batlle, A. Labarta, Finite-size effects in fine particles: magnetic and transport properties, J. Phys. D Appl. Phys. 35 (6) (2002) R15–R42.
[29] A. Demortiere, P. Panissod, B.P. Pichon, G. Pourroy, D. Guillon, B. Donnio, S. Begin-Colin, Size-dependent properties of magnetic iron oxide nanocrystals, Nanoscale 3 (1) (2011) 225–232.
[30] G.F. Goya, T.S. Berquó, F.C. Fonseca, M.P. Morales, Static and dynamic magnetic properties of spherical magnetite nanoparticles, J. Appl. Phys. 94 (5) (2003) 3520–3528.
[31] G. Balaji, R.A. Narayanan, A. Weber, F. Mohammad, C.S.S.R. Kumar, Giant magnetostriction in magnetite nanoparticles, Mater. Sci. Eng. B 177 (1) (2012) 14–18.
[32] R.R. Katti, Current-in-plane pseudo-spin-valve device performance for giant magnetoresistive random access memory applications (invited), J. Appl. Phys. 91 (2002) 10.
[33] J. Nogués, J. Sort, V. Langlais, V. Skumryev, S. Suriñach, J.S. Muñoz, M.D. Baró, Exchange bias in nanostructures, Phys. Rep. 422 (3) (2005) 65–117.

[34] X. Dong, M. Qi, Y. Tong, F. Ye, Solvothermal synthesis of single-crystalline hexagonal cobalt nanofibers with high coercivity, Mater. Lett. 128 (2014) 39–41.

[35] J. Xue, T. Wu, Y. Dai, Y. Xia, Electrospinning and electrospun nanofibers: methods, materials, and applications, Chem. Rev. 119 (8) (2019) 5298–5415.

[36] Y. Ji, X. Zhang, Y. Zhu, B. Li, Y. Wang, J. Zhang, Y. Feng, Nickel nanofibers synthesized by the electrospinning method, Mater. Res. Bull. 48 (7) (2013) 2426–2429.

[37] J.L. Storck, T. Grothe, A. Mamun, L. Sabantina, M. Klocker, T. Blachowicz, A. Ehrmann, Orientation of electrospun magnetic nanofibers near conductive areas, Materials 13 (1) (2019) 1.

[38] N. Fokin, T. Grothe, A. Mamun, M. Trabelsi, M. Klocker, L. Sabantina, C. Dopke, T. Blachowicz, A. Hutten, A. Ehrmann, Magnetic properties of electrospun magnetic nanofiber mats after stabilization and carbonization, Materials 13 (7) (2020) 7.

[39] D. Li, T. Herricks, Y. Xia, Magnetic nanofibers of nickel ferrite prepared by electrospinning, Appl. Phys. Lett. 83 (22) (2003) 4586–4588.

[40] T. Song, Y. Zhang, T. Zhou, C.T. Lim, S. Ramakrishna, B. Liu, Encapsulation of self-assembled FePt magnetic nanoparticles in PCL nanofibers by coaxial electrospinning, Chem. Phys. Lett. 415 (4–6) (2005) 317–322.

[41] Y.K. Sung, B.W. Ahn, T.J. Kang, Magnetic nanofibers with core (Fe$_3$O$_4$ nanoparticle suspension)/sheath (poly ethylene terephthalate) structure fabricated by coaxial electrospinning, J. Magn. Magn. Mater. 324 (6) (2012) 916–922.

[42] C.-R. Lin, T.-C. Tsai, M. Chung, S.-Z. Lu, Synthesis and characterization of magnetic nanoparticles embedded in polyvinyl pyrrolidone nanofiber film by electrospinning method, J. Appl. Phys. 105 (2009) 7.

[43] J. Xiang, X. Shen, F. Song, M. Liu, G. Zhou, Y. Chu, Fabrication and characterization of Fe–Ni alloy/nickel ferrite composite nanofibers by electrospinning and partial reduction, Mater. Res. Bull. 46 (2) (2011) 258–261.

[44] I.H. Chen, C.-C. Wang, C.-Y. Chen, Fabrication and characterization of magnetic cobalt ferrite/polyacrylonitrile and cobalt ferrite/carbon nanofibers by electrospinning, Carbon 48 (3) (2010) 604–611.

[45] J.A.C. Vanooijen, The effect of laminating permalloy flux guides in a thin-film magnetic recording head, J. Magn. Magn. Mater. 26 (1–3) (1982) 223–224.

[46] G.V.M. Williams, J. Kennedy, P.P. Murmu, S. Rubanov, Structural and magnetic properties of near surface superparamagnetic Ni$_{1-x}$Fe$_x$ nanoparticles in SiO$_2$ formed by low energy dual ion implantation with different fluences, Appl. Surf. Sci. 449 (2018) 399–404.

[47] X.Y. Zhang, Y. Liu, J. Li, X.J. Yang, Synthesis and magnetic studies of Fe–Ni nanofibres by electrospinning, Mater. Res. Innov. 17 (6) (2013) 436–439.

[48] Y.K. Du, P. Yang, Z.G. Mou, N.P. Hua, L. Jiang, Thermal decomposition behaviors of PVP coated on platinum nanoparticles, J. Appl. Polym. Sci. 99 (1) (2006) 23–26.

[49] D.T. Turner, A. Schwartz, The glass-transition temperature of poly(N-vinyl pyrrolidone) by differential scanning calorimetry, Polymer 26 (5) (1985) 757–762.

[50] T. Prakash, G.V.M. Williams, J. Kennedy, P.P. Murmu, J. Leveneur, S.V. Chong, S. Rubanov, Synthesis and structural, magnetic and magnetotransport properties of permalloy powders containing nanoparticles prepared by arc discharge, J. Alloy. Compd. 608 (2014) 153–157.

[51] B. Glaubitz, S. Buschhorn, F. Brüssing, R. Abrudan, H. Zabel, Development of magnetic moments in Fe$_{1-x}$Ni$_x$ alloys, J. Phys. Condens. Matter 23 (2011) 25.

[52] E.M. Abdelrazek, A.M. Abdelghany, S.I. Badr, M.A. Morsi, Structural, optical, morphological and thermal properties of PEO/PVP blend containing different concentrations of biosynthesized Au nanoparticles, J. Mater. Res. Technol. 7 (4) (2018) 419–431.

[53] X.G. Li, A. Chiba, S. Takahashi, Preparation and magnetic properties of ultrafine particles of Fe-Ni alloys, J. Magn. Magn. Mater. 170 (3) (1997) 339–345.

[54] A. Baldan, Review progress in Ostwald ripening theories and their applications to nickel-base superalloys - part I: Ostwald ripening theories, J. Mater. Sci. 37 (11) (2002) 2171–2202.

[55] A. López-Ortega, E. Lottini, C. d J. Fernández, C. Sangregorio, Exploring the magnetic properties of cobalt-ferrite nanoparticles for the development of a rare-earth-free permanent magnet, Chem. Mater. 27 (11) (2015) 4048–4056.

[56] G.C. Papaefthymiou, Nanoparticle magnetism, Nano Today 4 (5) (2009) 438–447.

[57] Z. Xu, C. Jin, A. Xia, J. Zhang, G. Zhu, Structural and magnetic properties of nanocrystalline nickel-rich Fe–Ni alloy powders prepared via hydrazine reduction, J. Magn. Magn. Mater. 336 (2013) 14–19.

[58] H. Wang, J. Li, X. Kou, L. Zhang, Synthesis and characterizations of size-controlled FeNi$_3$ nanoplatelets, J. Cryst. Growth 310 (12) (2008) 3072–3076.

[59] R. Nadarajah, L. Tasdemir, C. Thiel, S. Salamon, A.S. Semisalova, H. Wende, M. Farle, S. Barcikowski, D. Erni, B. Gokce, Formation of Fe-Ni nanoparticle strands in macroscopic polymer composites: experiment and simulation, Nanomaterials 11 (8) (2021) 8.

[60] N.A.M. Barakat, B. Kim, H.Y. Kim, Production of smooth and pure nickel metal nanofibers by the electrospinning technique: nanofibers possess splendid magnetic properties, J. Phys. Chem. C 113 (2) (2009) 531–536.

[61] N.A.M. Barakat, K.A. Khalil, I.H. Mahmoud, M.A. Kanjwal, F.A. Sheikh, H.Y. Kim, CoNi bimetallic nanofibers by electrospinning: nickel-based soft magnetic material with improved magnetic properties, J. Phys. Chem. C 114 (37) (2010) 15589–15593.

[62] O. Margeat, D. Ciuculescu, P. Lecante, M. Respaud, C. Amiens, B. Chaudret, NiFe nanoparticles: a soft magnetic material? Small 3 (3) (2007) 451–458.

[63] R.L. Edwards, The magnetic properties of evaporated nickel and iron films, Phys. Rev. 29 (2) (1927) 321–331.

[64] Y. Liu, Y. Chi, S. Shan, J. Yin, J. Luo, C.-J. Zhong, Characterization of magnetic NiFe nanoparticles with controlled bimetallic composition, J. Alloy. Compd. 587 (2014) 260–266.

[65] F. Bloch, Zur Theorie des Ferromagnetismus, Z. Phys. 61 (3) (1930) 206–219.

[66] C.M. Srivastava, R. Aiyar, Spin-wave stiffness constants in some ferrimagnetics, J. Phys. C Solid State Phys. 20 (8) (1987) 1119–1128.

[67] S. Larumbe, C. Gomez-Polo, J.I. Perez-Landazabal, J.M. Pastor, Effect of a SiO2 coating on the magnetic properties of Fe$_3$O$_4$ nanoparticles, J. Phys. Condens. Matter 24 (26) (2012) 266007.

[68] C. Vázquez-Vázquez, M.A. López-Quintela, M.C. Buján-Núñez, J. Rivas, Finite size and surface effects on the magnetic properties of cobalt ferrite nanoparticles, J. Nanopart. Res. 13 (4) (2010) 1663–1676.

[69] D.J. Zhang, K.J. Klabunde, C.M. Sorensen, G.C. Hadjipanayis, Magnetization temperature dependence in iron nanoparticles, Phys. Rev. B 58 (21) (1998) 14167–14170.

[70] S. Vitta, A. Khuntia, G. Ravikumar, D. Bahadur, Electrical and magnetic properties of nanocrystalline Fe$_{100-x}$Ni$_x$ alloys, J. Magn. Magn. Mater. 320 (3–4) (2008) 182–189.

[71] B.E. Argyle, S.H. Charap, E.W. Pugh, Deviations from T32 law for magnetization of ferrometals: Ni, Fe, and Fe+3% Si, Phys. Rev. 132 (5) (1963) 2051–2062.